Nanoscale Advances

ROYAL SOCIETY OF CHEMISTRY

PAPER

View Article Online
View Journal | View Issue

Cite this: *Nanoscale Adv.*, 2025, **7**, 3322

Gold–silver alloy nanoparticle formation *via* spark ablation: the dynamics of material mixing†

Attila Kohut, *[a] Lajos Péter Villy,[a] Linnéa Jönsson, [b] Dániel Megyeri, [a] Gábor Galbács, [c] Maria E. Messing [b] and Zsolt Geretovszky[a]

Binary nanoparticles (BNPs), composed of two distinct materials, offer tailored properties advantageous for various applications, including enhanced catalytic, magnetic, and optical behavior. Among the synthesis methods for BNPs, spark ablation stands out for its capability to produce multicomponent nanostructures with tunable compositions. This study investigates the mixing dynamics of material vapors in spark ablation, a critical step in the process of BNP formation. Using spatially and temporally resolved optical emission spectroscopy (OES), we track the expansion and interaction of gold and silver vapors within the spark gap of a spark discharge generator. The collected data reveal the evolution of the vapor mixing process, complemented by a quantitative model that maps the variation of the gold-to-silver concentration ratio over time and space. We correlate these observations with the composition distribution of synthesized AuAg BNPs, as analyzed by scanning transmission electron microscopy (STEM) with energy-dispersive X-ray spectrometry (EDX). Our findings elucidate key factors influencing the compositional variance of BNPs, facilitating the understanding of the role of vapor mixing in achieving well-controlled particle processes *via* spark ablation.

Received 28th December 2024
Accepted 2nd April 2025

DOI: 10.1039/d4na01076k

rsc.li/nanoscale-advances

Introduction

Binary nanoparticles (BNPs) are composed of two different materials, exhibiting unique properties that can be tailored for specific applications. By combining distinct elements, enhanced properties can be achieved that are not possible with individual components. Examples would include improved catalytic activity, magnetic behavior, and optical properties compared to their single-component counterparts.[1–3] Although many strategies exist for producing BNPs, including chemical synthesis,[4] lithography,[5] flame synthesis[6] or laser ablation,[7] one aerosol synthesis route of particular potential is spark ablation.[8,9] The process of producing multicomponent nanostructures *via* spark ablation is usually referred to as spark mixing.[8] It is based on the periodic ablation of two non-insulating electrodes by a spark plasma, repetitively ignited in a controlled, flowing gaseous environment.[10–14] The technique was shown to be scalable in terms of particle yield, either *via* parallelizing of multiple ablation sources, or *via* increasing the spark repetition rate to the kHz regime.[15] There are several variations of the technique, depending on whether the mixing occurs within a single spark discharge generator (SDG), or aerosols coming from separate generators are mixed outside of their sources.[15] The first approach, *i.e.*, the so-called atomic-scale mixing is predominantly employed in the field, due to its enormous capabilities in producing multicomponent particles of various materials with tunable composition and crystal structure.[16–21] This method is primarily facilitated by the fact that SDGs employ sparks with oscillatory current and voltage characteristics, which results in the alternating ablation of the two electrodes, thus transferring both electrodes' material into the interelectrode space (the so-called spark gap). This process sets the basis of BNP formation, which then proceeds due to the fast expansion and concomitant cooling of the material vapor. The ability of sparks to produce mixed phases of various materials systems has been reported, including those are well miscible in bulk[20,22] as well as materials which have miscibility gaps,[23] even for more than two components.[16,24] In addition to the obvious advantages of such a powerful method, there are several characteristic features of spark mixing that are generally accepted to be part of the process. The most notable one is the broadness of the composition distribution of the generated BNPs. It was shown in the earliest reports on spark mixing that the relative standard deviation of the particle composition can reach more than 50%.[22,23] Feng *et al.* provided a semi-quantitative understanding of this phenomenon, *via* arguing that incomplete vapor mixing can lead to the formation of single-element primary particles, which will coalesce later into

[a]*Department of Optics and Quantum Electronics, University of Szeged, Dóm sq. 9, Szeged, 6720, Hungary. E-mail: kohut.attila@szte.hu*

[b]*Solid State Physics and NanoLund, Lund University, Professorsgatan 1B, Lund, 221 00, Sweden*

[c]*Department of Molecular and Analytical Chemistry, University of Szeged, Dóm sq. 7-8, Szeged, 6720, Hungary*

† Electronic supplementary information (ESI) available. See DOI: https://doi.org/10.1039/d4na01076k

binaries.[25] This idea seemed to be supported by several studies employing alloyed or sintered (thus "premixed") electrodes – hence naturally ensuring a complete spatial overlap between the different material vapors – resulting in much smaller, about or even less than 10%, relative standard deviations.[26,27] Other reports used dissimilar, single-element electrodes, but applied various geometric constraints on the emerging vapor plumes to facilitate more complete mixing and thus achieved lower variability in the BNP composition (even down to 1% relative standard deviation).[16,28] These indirect results suggest that the complete mixing of the atomic material vapor – or the lack of it – has a decisive role in determining the composition distribution of the synthesized BNPs. Nevertheless, the direct observation of the mixing dynamics of the material vapors has not been carried out so far, which would provide direct evidence on the mixing state of the system at various points and time. In the present work, we employ spatially and temporally resolved optical emission spectroscopy (OES) to provide the evolution of the light emitted by gold and silver atoms ablated from two single-element electrodes in an SDG. The data is used to qualitatively follow the expansion dynamics of the gold and silver vapor along the horizontal axis of the spark gap and thus provide an improved understanding on the timescale of the mixing process. Moreover, we use a quantitative model, specifically developed for this task,[29] to deduce the spatial and temporal variation of the gold-to-silver atomic ratio inside the spark gap. These data will be compared to the composition distribution of the generated AuAg BNPs, determined from single-particle scanning transmission electron microscopy (STEM) with energy-dispersive X-ray spectrometry (EDX). The data will be used to outline a qualitative picture describing the key factors, which determine the relative standard deviation of the BNP composition.

Materials and methods

The details of the particle generator setup we used in the present study have been described elsewhere.[21] For most of the experiments, we used an Au and an Ag electrode (both 99.99% purity, Goodfellow Cambridge Ltd.) and AuAg alloy electrodes for control experiments (50 at% Ag composition, 99.99% purity, ChemPUR GmbH.). Both electrodes were cylindrical and had a diameter of 3.0 mm. Ar carrier gas (99.996% purity, Messer Hungarogáz Kft.) was used with a 5 L min^{-1} flow rate, while atmospheric pressure was maintained inside the generator chamber. To acquire plasma emission from a well-defined spatial region from the spark gap, we employed a specific light-collection setup. First, the plasma light was imaged using an 80 mm diameter lens with a 100 mm focal length and a magnification of 1.2. The imaged light was then directed onto a slit with dimensions of 200 μm width and 3.0 mm height. Behind the slit, we placed a multimode optical fiber (silica fiber with a 50 μm core and 0.22 numerical aperture, SFS50/125Y from Thorlabs GmbH) equipped with a collimating lens (Avantes COL-UV/vis). This arrangement allowed us to collect light passing through the optical system while limiting the collection area to the defined spatial region. The slit ensured spatial resolution along the electrodes' axis while integrating plasma light perpendicular to this axis, effectively averaging out variations caused by spark positional instability. The second lens, positioned at the focal point of the optical fiber, provided a very small overall numerical aperture. Although this reduced the collection efficiency, it prevented "cross-talk" between different spatial regions along the gap. The collected light was transmitted to an Echelle spectrograph (Mechelle 5000, Andor Technology Ltd.) coupled with a nanosecond-gated intensified CCD (ICCD) detector (iStar-734 Gen 2 (W-AGT, -03), Andor Technology Ltd.). This setup allowed us to collect spectra in the 300–800 nm range, achieving temporal and spatial resolutions of 500 ns and approximately 170 μm, respectively, with a resolving power of about 5000. A schematic figure on the experimental setup and on the concept of the temporally and spatially resolved OES investigation of the spark plasma along with further experimental details can be found in the ESI.†

For particle characterization, the generated nanoparticles were deposited onto TEM grids by using a low-pressure inertial impactor. The grids were transferred in ambient conditions to a JEOL 3000 F TEM equipped with an EDX system for analysis of the composition of single particles using STEM-EDX. The Inca software package (Oxford Instruments) was used for collecting point spectra of 30 individual particles for each sample at a magnification of 1 000 000× to 2 000 000×. The spectra were collected for 60 seconds, corrected for density and thickness, and quantified using the Au and Ag L-peaks in the Inca software. The size of the analyzed particles was determined from STEM images acquired before collecting the spectra.

Results and discussion

Considerations on the mixing process

To describe the BNPs generated as a result of the spark mixing process the two most important parameters that need to be considered are the average composition – often expressed as the atomic percentage of one of the components, here Ag, for instance – and the variability of the composition on a single particle level. These parameters can mathematically be expressed as the mean and the standard deviation (SD) of the composition distribution of the generated BNPs, respectively. The particles are commonly characterized by a single average composition value, determined by ensemble techniques such as ICP-MS or XRF, while a more thorough analysis on both the mean and the SD can be given by STEM-EDX[27] or alternatively by single-particle ICP-MS.[19] When two dissimilar pure electrodes are employed in an SDG, it is assumed that the average composition is mostly determined by the relative erosion rate of the two electrodes.[20,25] This implies that the plasma stoichiometry – *i.e.*, the ratio of the two material components – determined by the ablation process is preserved in the forming binaries. Consequently, the mean composition is assumed to be the same throughout the whole particle formation process, including the initial vapor, the primary spherical particles and the final aggregates as well. However, the particle-to-particle variability of the composition, *i.e.*, the SD of the mean, will vary during particle evolution. The exact SD value of the final NPs

will depend on the mixing process, but a simplified description can be given by following similar considerations to that of Feng *et al.*[25] According to this, if we consider some "smallest units" of pure Au and Ag particles, and assume that every two particles can collide and attach to each other with a given – constant – probability, the variation of SD of the composition (denoted as SD_φ in the rest of the text) can be given by the following formula:[25]

$$SD_\varphi = \sqrt{\frac{\overline{\varphi}(1-\overline{\varphi})}{N}} \quad (1)$$

The collision probability is related to the "availability" of colliding partners, that is the average atomic composition ($\overline{\varphi}$), assumed above to be constant throughout the particle formation process. N is the number of smallest pure units in the final BNPs. N is proportional to the cube of binary NP size/unit size ratio. To exemplify the effect of the unit size on SD_φ, we consider two cases here. For both cases we use an Ag content of 0.5, expressed in atomic ratio, defined as the number of silver atoms divided by the total number of atoms. First, let's consider perfect atomic mixing, when the colliding partners are the Au and Ag atoms, hence the unit diameter is *ca.* 0.15 nm. To account for a minor uncertainty in size we consider the standard deviation of the unit diameter (denoted as SD_D) to be 0.02 nm. The second case is the other extreme, which is a perfectly unmixed vapor, where pure Au and Ag primary particles can form without incorporating any atoms from the other element. In this case we consider the primaries to be the smallest units having a size of 4.0 nm with a 0.5 nm SD_D, which is about the primary particle size for the AuAg BNPs generated in our system. As an attempt for a more generalized discussion, we plot the relative standard deviation (RSD), defined as the SD_φ divided by the mean Ag composition expressed in percentage, in Fig. 1.

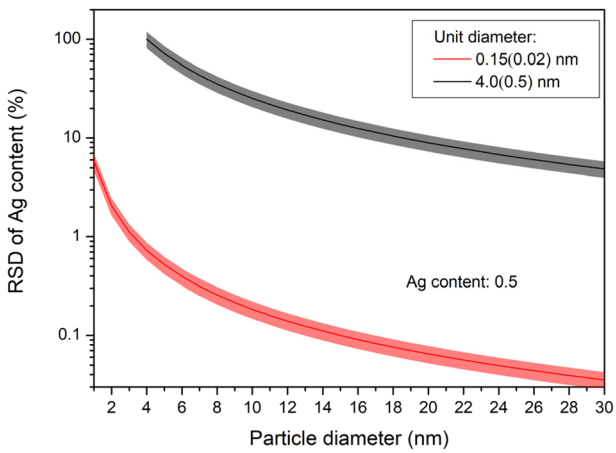

Fig. 1 The variation of RSD as a function of (final) particle diameter at two different unit diameters. The shadowed areas around the lines represent the uncertainty due to the uncertainty in the unit particle diameter. Please note the logarithmic scale in the vertical axis.

The general trend shown in Fig. 1 is that the RSD of the composition distribution for a given BNP size will decrease for larger sizes, which means that larger particles will be more uniform in composition. This is expected, considering the "averaging" effect of having more units in a single particle. This already leads to a practical conclusion, namely that for precise characterization of the composition distribution of a given particle population, monodisperse fractions should be treated separately. By looking at the values of Fig. 1, it is apparent that if Au and Ag atoms can nucleate independently and grow up to their largest spherical size and only start mixing afterwards, each BNP will contain only a small number of pure units, therefore the variation of the composition of individual particles will be very large. In this case, the RSD will be *ca.* 10% even for binaries as large as 30 nm in diameter, and close to 100% for the smallest particles. The other extreme case is the opposite: perfect atomic-level mixing is characterized by very small RSD (<5%) even for particles of around 1 nm in diameter and well below 0.1% for particles of a few tens of nanometers in diameter. This is understandable considering the relatively large number of atoms in the BNPs.

It is plausible to assume that the closest experimental realization of perfect atomic mixing for the Au–Ag materials system is the use of AuAg alloy electrodes. Since Au and Ag form a solid solution in bulk at every composition and have similar thermal properties, Au and Ag atoms most likely will coexist in every point in time and space during spark ablation. Our previous OES investigation of a spark plasma in the vicinity of an AuAg alloy electrode with 0.5 Ag content right after the ablation stage resulted in an Au-to-Ag number concentration ratio of *ca.* 1, which supports the above assumption.[29] The composition of BNPs generated from alloyed AuAg electrodes has recently been investigated thoroughly, and for 0.5 nominal composition an SD_φ of 0.02 was reported, which translates to an RSD of 4%.[27] This data corresponds to size-selected 20 nm particles, where the expected RSD is very low – below 0.1% – in case of perfect mixing (*cf.* Fig. 1). This suggests that the achievable precision of AuAg BNP composition determination is limited by the capabilities of the STEM-EDX technique. To further support this idea, we synthesized 0.5 Ag content AuAg BNPs from alloyed electrodes and measured the composition distribution of monodisperse fractions in the range of *ca.* 9–15 nm in diameter. The total number of analyzed particles was 29. The obtained RSD values varied between 3.4 and 5.9%.

By plotting the corresponding RSDs – together with one value from[27] – the data scatter around a constant value even though the theoretical curve predicts a clearly decreasing RSD (*cf.* Fig. 2A). This also suggests that the obtained RSDs do not represent the actual mixing process, instead, they roughly imply the lower limit achievable with the particle characterization setup. We consider the average of these values – 4% – to be representative for the RSD of particle composition measurement in the present case. It should be noted that the obtained values are perfectly in line with the generally accepted maximum accuracy of EDX – *ca.* ±0.02 in atomic ratio[30] – which further supports our statement that the predicted very small RSDs cannot be resolved due to experimental limitations.

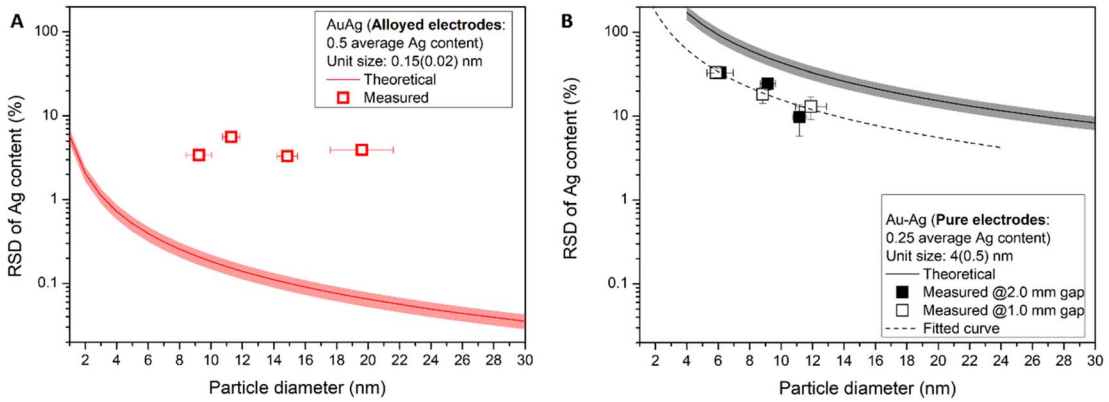

Fig. 2 Comparison of the measured variation of the RSD of the Ag content for 0.5 average Ag content AuAg particles (squares) with the theoretically expected curve (continuous line) in case of perfect atomic mixing (A). Measured RSD of the Ag content of AuAg particles synthesized with pure Au and Ag electrodes at 1.0 mm and 2.0 mm gaps (B). The graph indicates the theoretical curve (continuous black line) for a mean composition of 0.25 and 4(0.5) nm unit size. The dashed line is the result of fitting eqn (1) to the measured data.

To further investigate the material mixing in case of inherently non-overlapping material vapors, alloyed AuAg BNPs were generated from pure Au and Ag electrodes at two different interelectrode gaps. Fig. 3 illustrates the result of the STEM-EDX analysis of 30 individual particles obtained at a 2.0 mm gap setting. It can be seen in Fig. 3A that the average Ag content is 0.254 with an SD_{φ} of 0.079. This translates to a *ca.* 31% RSD, which is a relatively large value. The corresponding average particle diameter is 9.5 nm, with an SD_D of 3.2 nm (see Fig. 3B). Elemental maps shown in Fig. 3D and E were taken from larger individual particles – with a diameter of 20 nm – indicating the homogeneous distribution of Au and Ag atoms inside the particles. This is in accordance with the very good miscibility of gold and silver, which will result in the formation of homogeneously mixed particles, even if the colliding sub-units had different compositions. It should be noted that the composition distribution of individual particles obtained at 1.0 mm gap was very similar to that of the 2.0 mm gap setting, with a mean and SD_{φ} of 0.265 and 0.067, respectively. However, as apparent from eqn (1) and the corresponding discussion above, the SD_{φ} should

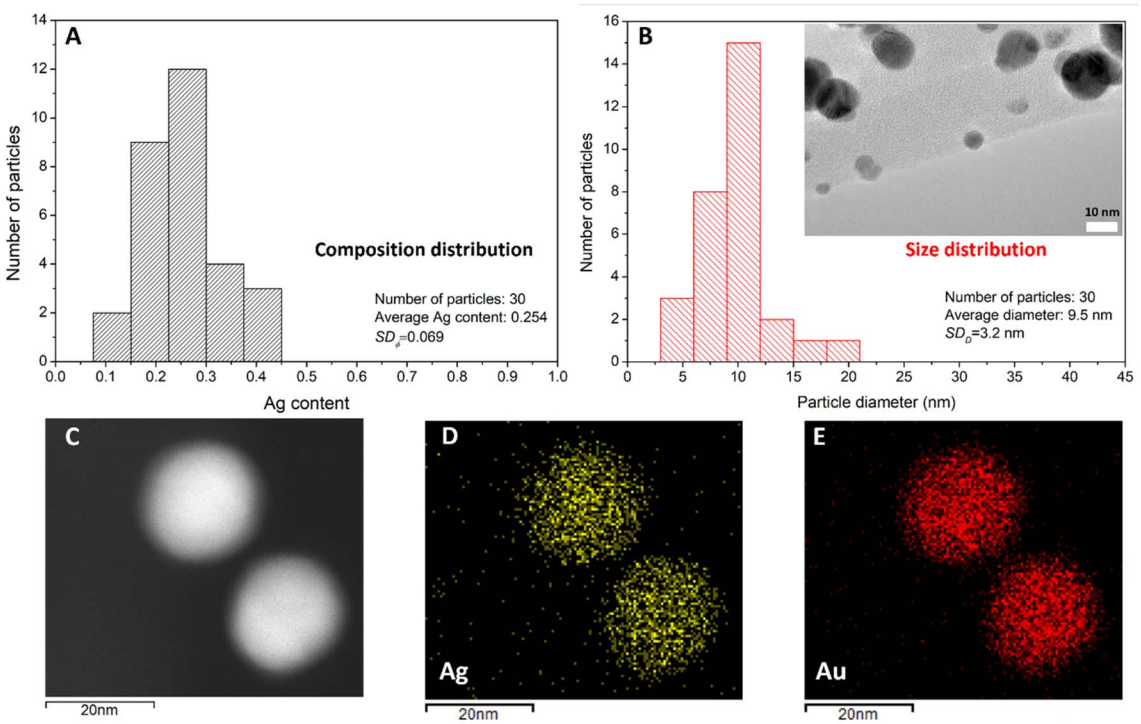

Fig. 3 Distribution of Ag content within AuAg BNPs synthesized from pure Au and Ag electrodes with a 2.0 mm gap (A). Size distribution of the generated BNPs, with a TEM micrograph in the inset (B). STEM micrograph and EDX elemental maps of two AuAg BNPs with 20 nm diameter (C–E).

Table 1 Average diameter, SD_D, average Ag content, SD_φ, and RSD of different particle size-groups within the AuAg samples synthesized at 1.0 mm and 2.0 mm spark gaps

Average diameter (nm)	SD_D (nm)	Average Ag content	SD_φ	RSD of the Ag content (%)	Number of particles in the subgroup
2 mm gap					
6.13	0.99	0.177	0.058	32.9	8
9.15	0.80	0.262	0.064	24.5	13
11.17	0.41	0.280	0.028	9.9	6
1 mm gap					
5.87	0.90	0.221	0.073	33.0	11
8.82	0.58	0.283	0.052	18.3	12
11.90	1.07	0.305	0.040	13.1	7

depend on the particle size, so instead of using the sample-averages we divided the analyzed particles – with a total number of 57, corresponding to the results for both 2.0 and 1.0 mm gaps – into subgroups depending on their size. These subgroups represent close-to-monodisperse fractions, the average diameters, SD_Ds, average compositions, SD_φs, and RSDs of which are summarized in Table 1.

Data shown in Table 1 agree well with the qualitative picture discussed above, predicting smaller SD_φs for larger particles. It should be noted that there is some variation in the average composition of the subgroups as well. This variation is within the corresponding SD_φs and might be attributed to the relatively small sub-sample size. Nevertheless, to characterize each subgroup we use the RSD of the Ag content – expressed in % – instead of the absolute values, in order to take into account the deviation from the average value and also to be consistent with our previous discussion above.

RSD data from Table 1 are plotted in Fig. 2B together with the theoretical curve predicted by eqn (1) for a unit size of 4(0.5) nm, representing completely unmixed vapors. As can be seen in Fig. 2B, the experimental data follows a very similar trend to that of the theoretical prediction for unmixed vapors, but with consistently lower RSD values. By fitting the data with eqn (1) an – effective – unit size of *ca.* 2 nm is obtained (please see the dashed curve in Fig. 2B). The above results have several implications: (i) by using pure Au and Ag electrodes, the generated AuAg alloy nanoparticles' composition distribution clearly exhibits size-dependent RSD – in the range of *ca.* 10–33% – which is well above the *ca.* 4% RSD corresponding to alloy electrodes, considered to represent the experimental accuracy (*cf.* Fig. 2A and B). (ii) The RSD qualitatively follows the same trend as predicted by eqn (1), but the absolute values indicate that the vapor-mixing is neither complete, nor uncomplete. (iii) Even though the simple eqn (1) considers distinct pure particles with a given unit size, we assume that particle mass – or number of atoms – is preserved, so any intermediate state of mixing can be formally treated by considering pure particles with an effective unit size between 0.15 nm and 4 nm. Therefore the *ca.* 2 nm effective size obtained from fitting eqn (1). to the experimental data implies that the Au and Ag vapors partially mix before the *ca.* 4 nm diameter primaries could form and aggregate into larger particles. In order to better understand the processes leading to this partial mixing, temporally and spatially resolved OES methods were employed to track the evolution of the – light emitting – Au and Ag vapors.

Following the mixing dynamics *via* OES

Spark plasma formation is well known for the concomitant intense UV-vis line emission originating predominantly from the excited species – atoms and ions – present in the spark gap. This emission holds valuable information on the main plasma properties, such as temperature and electron concentration, as well as the temporal and spatial distribution of the emitting species.[31] OES and OES-based plasma diagnostic methods in particular aim at deriving these information.[8] In the context of BNP synthesis, a very important stage of spark plasma emission is the so-called afterglow, which follows the relatively short current-conducting arc stage – in which electrode ablation occurs.[32] In the afterglow, the plasma emission is dominated by the neutral atoms in the electrode material vapor – together with the atoms of the carrier gas – hence it provides temporal and spatial information on the ablated material vapor.[31,32] It should be noted that this type of information can only be extracted by means of OES until the temperature is high enough to promote the presence of excited species and the vapor is not diluted beyond a certain level, so until the number concentration of the emitting species does not become too low. Previous studies show that the temporal window for investigating the afterglow stage by means of OES is about 25 μs wide, depending on the conditions.[31] Since atomic emission is characteristic to the respective emitting elements, by adequate instrumentation, acquiring the emission spectrum of the spark plasma allows for reconstructing the temporal and spatial evolution of the material vapor ablated from the two electrodes.

We used the experimental setup detailed in the Materials and methods section and in the ESI† to follow the temporal and spatial variation of several atomic spectral lines of Au and Ag (with spectroscopic notation: Au I and Ag I, respectively), for the details please see Table S1.† Fig. 4A shows the normalized and averaged intensities as a function of the axial position of the emission acquisition, 4.2 μs after the onset of the breakdown. As can be seen in the current and voltage characteristics of the spark (see Fig. S3†), this temporal point approximately sets the beginning of the afterglow stage, *i.e.*, represents the time when

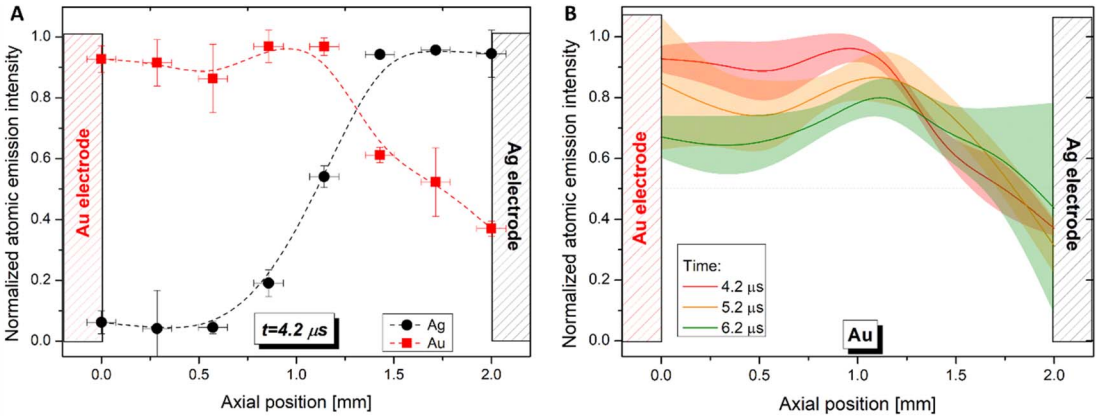

Fig. 4 Spatial distribution of atomic emission intensity of Au and Ag atoms along the spark gap 4.2 μs after the onset of the breakdown (A). Temporal variation of the spatial intensity distribution of Au atomic emission intensity (B). Measured points are connected to guide the eye.

material ablation has already occurred, and Au and Ag vapor has been released into the spark gap. As evidenced by Fig. 4A, emission intensities corresponding to Au and Ag atoms exhibit very distinct distributions, indicating a mixing state far from being complete (the position of Au and Ag electrodes is schematically indicated in Fig. 4 for reference). Ag I emission is practically unmeasurable in the vicinity of the Au electrode at this time, meaning that the ablated Ag vapor has not reached the opposing Au electrode yet. On the details of the preparation of Fig. 4 please see the ESI.†

The spatial evolution of the Au I emission in the spark gap at different times is shown in Fig. 4B. It can be qualitatively seen how the emitting Au atoms gradually approach the Ag electrode. This data can be used to determine the velocity of the Au and Ag vapor jets, as shown in Fig. 5. To construct this figure, the spatial spectral intensity distribution curves (some of them shown in Fig. 4) were used. The axial position corresponding to the 50% of the maximum intensity (which is always 1, due to normalization) was determined at every temporal point. These data are plotted in Fig. 5. Please note that the error bars represent the uncertainty due to the temporal and spatial resolution of our experimental setup. It can be seen that the Au vapor jet has a *ca.* 36% higher velocity than that of the Ag vapor jet. Please note that this velocity represents the first few microseconds of the measurement, which corresponds to the material ablation stage, the movement of the vapor front slows down afterwards, as evidenced by the points not included in the linear fit in Fig. 5. It should be mentioned that usually a much faster material release – in the order of 1000 m s^{-1} – is assumed during spark ablation, mostly based on the early OES measurements of Cundall and Craggs.[33] Those measurements were performed in different experimental conditions and with different metal electrodes, though, so direct comparisons are hard to make. Nevertheless, one general conclusion, which holds for all the metals investigated in their study was that the vapor jet originating from the initially anodic electrode always has higher velocity, than that of the cathode jet. This observation is in line with our results, showing a lower velocity for Ag, which is initially cathodic in our experiments. Even with this relatively low velocity, some fraction of the Ag vapor plume reaches the opposing Au electrode in roughly 10–15 μs, so it is safe to say that according to the emission intensity distribution of the Au and Ag atoms, the mixing of the metal vapors is starting to occur well within the afterglow stage, *i.e.*, before the plasma cools down to ambient temperature.

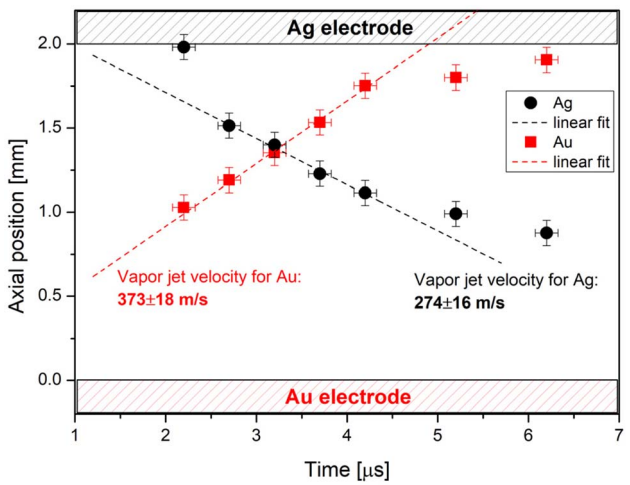

Fig. 5 Movement of the Au and Ag atomic vapor between the two electrodes as represented by the atomic emission intensity. The fitted lines are used to estimate the vapor ejection velocity for Au and Ag for the respective electrodes. The position of the electrodes is indicated for reference.

The above results provide a qualitative understanding of the atomic mixing process, based on the variation of the optical emission spectrum of the spark plasma. However, the actual mixing state of the Au and Ag vapors remains to be unknown, because the atomic intensity ratio does not directly represent the actual plasma composition. To gain a deeper insight into the mixing state of the vapors, we recently developed a quantitative model to determine the Au/Ag number concentration ratio – including both atoms and ions – from the emission spectra.[29] We have shown that temporally and spatially resolved emission spectra – acquired with the same experimental setup

employed in the present work – can be used to calculate the concentration ratio of the electrode elements with a relative error of about 15%. For the details of the method please refer to the original paper. We have used this technique to derive the temporal variation of the Au/Ag concentration ratio – which is, for more straightforward comparison with particle composition data, expressed as $N_{Ag}/(N_{Au} + N_{Ag})$ – at different positions in the gap.

It can be seen in Fig. 6 that short after the breakdown – at about the beginning of the afterglow stage – the electrode material is still very unevenly distributed in the gap. Near the Ag electrode the metal vapor mostly contains silver (*ca.* 70%), while only about 5% silver is present near the Au electrode. The center of the gap is also rich in gold. On one hand, this proves that mixing is not "instantaneous" on the relevant timescale, and on the other, it shows that Au atoms spread faster in the gap than that of the Ag atoms, which is in line with the ejection velocity difference shown in Fig. 5. Fig. 6 also shows that equilibration takes place rather rapidly, since the silver content converges roughly to the same values between about 0.18 and 0.25 at every point along the gap. A reasonably homogeneous metal distribution will prevail in *ca.* 20–25 μs after the onset of the breakdown. This indicates a well-mixed vapor state along the electrodes' axis. It is important to note here that the obtained equilibrium Ag content matches well the sample-average of the generated AuAg NPs, which was 0.254(0.079) (*cf.* Fig. 3). This proves the important assumption that the Au-to-Ag ratio is preserved from ablation to particle formation. It should also be stressed that even though complete vapor mixing does not occur instantaneously, mixing does take place in a relatively short period of time, well before the plasma cools down, thus before the onset of nucleation.

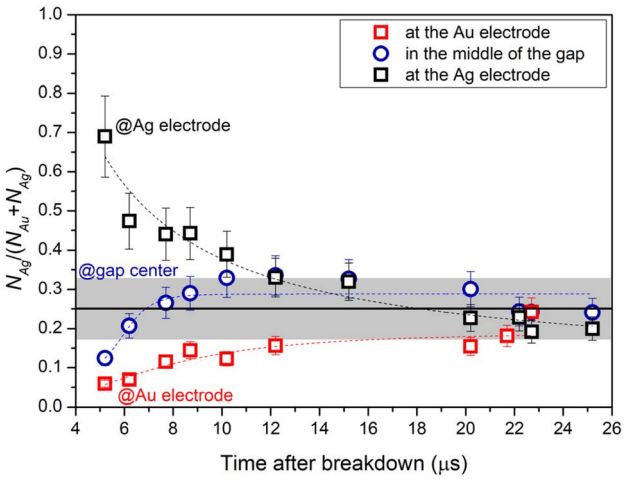

Fig. 6 Variation of the plasma composition – defined as the Ag content in atomic ratio – in time at different positions along the spark gap. The black line indicates the average composition of the AuAg BNPs forming under the same conditions, with a grey zone representing the SD_φ of the obtained composition distribution. The positional accuracy of the light collecting slit is estimated to be not worse than 85 μm.

The OES results suggest that along the electrodes' axis, there is no essential difference between the case of having a pair of alloyed AuAg electrodes and two pure Au and Ag electrodes in the sense that Au and Ag atoms coexist during every relevant stage of particle formation. However, there is a fundamental difference between the two cases: in case of alloyed electrodes, the well-mixed state prevails from the very beginning of the ablation process, since the vapor plumes overlap and expand together. For dissimilar electrodes, the well-mixed state is achieved in a short, but non-zero time, while the gold and silver vapor expand in different directions independently. This can schematically be seen in Fig. S2.† Therefore, a further factor that needs to be taken into account is the potential movement of the metal atoms perpendicular to the electrodes' axis. The information content of the present data is limited in this regard, because on one hand, the intensity emitted by these atoms is averaged out due to spatial integration by a lens, and on the other, there is an upper limit of the investigated spatial area due to the height of the slit used (please see the Materials and methods section). This means that our measurement data does not hold information on the composition of regions further away from the electrodes' axis than that of the radius of the electrodes. As proved by the data shown in Fig. 6, gold-rich and silver-rich regions exist near the gold and silver electrodes, respectively, shortly after the ablation stage. If metal vapor fractions from these regions could diverge from the gap before reaching the well mixed state along the electrodes' axis (*ca.* 20–25 μs), that could lead to the formation of primary particles with a broad composition distribution, similarly to that of a completely unmixed case. In order to assess this possibility, we need to compare the velocities relevant to this process. The velocity of the gas flow around the spark gap is much lower than that of the vapor ejection velocity – by *ca.* two orders of magnitudes[13] – therefore it does not have any considerable effect on vapor movement in the relevant timescale. However, the plasma expansion velocity is known to be in the same order of magnitude as the vapor ejection velocity.[34] We performed further high-speed imaging measurements to confirm that the expansion velocity is in the range of a couple of hundred m s^{-1} (for details please see the ESI†). This means that on the timescale of mixing (*ca.* 20–25 μs) partially mixed or completely unmixed fractions of the vapor can leave the gap, before reaching the equilibrium plasma composition shown in Fig. 6. It is hard to quantify the portion of these fractions with respect to those remaining in the gap and thus mix completely. A rough geometric estimate can be given on the non-overlapping trajectories based on the approximate average velocities, the size of the gap and the time of complete mixing. This suggests that around 20–25% of the total vapor leaves the gap without reaching the well-mixed state, which is non-negligible. Such a scenario would lead to an intermediate overall mixing state both promoting the formation of primaries mixed on the atomic scale – originating from the gap region – and primaries predominantly containing one of the two constituents – originating from the outer regions. As a result, the particle growth and aggregation process would set off in an environment where the gold-to-silver ratio is not homogeneously distributed among

the individual particles. Even though eqn (1) is unable to quantitatively describe such a complex mechanism, it should still correctly predict the scaling of the RSD with particle size. As shown in Fig. 2B, eqn (1) fits decently the experimental particle composition data, providing an average effective primary size – ~2 nm, which is *ca.* one order of magnitude larger than that would characterize perfect atomic mixing – that is *ca.* 0.15 nm. This is in line with the proposed mechanism of the mixing process as described above based on OES-based plasma diagnostics.

One comment should be made here on the potential effect of material transfer between the electrodes on the mixing process and the average composition of the BNPs. At the conditions of the experiments presented in this study with a 2.0 mm gap no signs of significant material transfer were observed. This is also indicated by Fig. 4 and 5, since in case of the presence of a gold layer on the silver electrode – due to the much higher ablation rate of gold, this is the expected scenario – the gold atoms should be much more evenly distributed in the gas from the very beginning of the ablation stage. However, in case of a 1.0 mm gap, we observed signs of material transfer from the gold to the silver electrode. Following our argument above, such a situation should lead to a better spatial overlap between gold and silver atoms during ablation – at least on one side of the gap, which should push down the effective size of poorly-mixed subunits. Therefore, qualitatively, a smaller variability in the particle composition would be expected. If we compare the average SD_{φ} of Ag content in case of 2.0 mm and 1.0 mm gaps, which are 0.079 and 0.067, respectively, we do see a slight decrease. This decrease can qualitatively be explained by the result of material transfer between the gold and silver electrodes.

A practical implication of our findings is that the vapor expansion perpendicular to the electrodes' axis might play a key role in determining the broadness of the composition distribution of the generated BNPs. This implication is already in line with literature results reporting on exceptionally good compositional uniformity. In the work of Ortiz de Zárate *et al.* AuAg NPs of *ca.* 5 nm in diameter were synthesized from pure electrodes and exhibiting an RSD around 2%, which is much lower than the values obtained in the present study or in.[27] Please note that the 2% value is our estimation based on the data given in.[28] They, however, instead of the common rod-to-rod electrode geometry with a freely expanding vapor plume – as used here and in[27] – used a special arrangement with a funnel-like "particle collector" to force the material vapor into a limited volume. Due to this geometric constraint, it is plausible to assume that the formation of unmixed vapor zones was effectively inhibited and thus the variability of the particles initial composition was strongly decreased, leading to a very small RSD even at 5 nm particle size.

Conclusions

This study explores the so-called spark mixing process in the case of the gold-silver materials system. AuAg BNPs were synthesized and characterized in terms of their composition distribution both for alloyed AuAg and pure Au and Ag electrodes. The relative standard deviation of the obtained samples was analyzed as a function of particle size by employing a simple statistical model. It has been shown that the RSD of AuAg BNPs synthesized by using pure Au and Ag electrodes show a clear size-dependent trend in agreement with the mathematical model, indicating an intermediate state between complete atomic mixing and the formation of pure Au and Ag primary particles. To better understand the processes leading to the obtained BNP properties, spatially and temporally resolved OES was employed to map the gold and silver atomic vapor distribution and its evolution along the electrodes' axis. Our findings reveal that vapor mixing occurs in about 20–25 μs after the breakdown, achieving an equilibrium gold-to-silver ratio along the axis. The obtained silver content is in good agreement with the average silver content of the generated BNPs, indicating that the BNP composition is indeed predominantly dictated by the relative erosion rate of the electrodes and the ratio of the ablated electrode material is preserved during the whole particle formation process. However, even though the gold and silver vapors are well mixed in the spark gap even before the plasma cools down, the compositional variability of the AuAg BNPs is rather large, characterized by a *ca.* 33% RSD for the smallest, 6 nm particles and *ca.* 10% for the largest, 11 nm particles. This inhomogeneity was attributed to the rapid expansion of the plasma in a direction perpendicular to the electrodes' axis, which causes some fractions of the distinct gold and silver vapors emerging from the opposing electrodes to diverge away before mixing. Such a process would lead to greater variability in the composition of primary particles, in good qualitative agreement with the predictions of the simple mathematical model used here. These findings also imply that larger, size-selected BNPs will naturally exhibit a narrower composition distribution. If the synthesis of BNPs with homogeneous composition is aimed in the few nanometers range, the primary size of already mixed AuAg particles should be pushed down to the sub-nm level. Our results suggest that this can be achieved by applying geometric constraints on the expanding material vapors, which will limit their free expansion away from the spark gap. There are multiple experimental reports in the literature showing that such an approach is favorable in achieving highly homogeneous BNPs, to the mechanism of which our study provides a detailed understanding, enabling more rational and further optimized SDG designs in the future.

Data availability

Data for this article, including raw OES datasets and measured particle composition data are available at Zenodo at **https://doi.org/10.5281/zenodo.14229738**. Further data supporting this article have been also included as part of the ESI.†

Conflicts of interest

The authors declare no competing interests.

Acknowledgements

We are grateful for the funding provided from the National Research, Development and Innovation Fund under the PD_21 OTKA (project PD 139077) and under the 2022-2.1.1-NL Creation of National Laboratories, Complex Development funding schemes (project 2022-2.1.1-NL-2022-00012). Research leading to these results has also received funding from the K 146733 (OTKA) project and was also supported by the Swedish Foundation for Strategic Research (Grant No. FFL18–0282).

References

1 M. Rebello Sousa Dias and M. S. Leite, *Acc. Chem. Res.*, 2019, **52**, 2881–2891.
2 X. M. Lin and A. C. S. Samia, *J. Magn. Magn. Mater.*, 2006, **305**, 100–109.
3 Y. Sun and S. Dai, *Sci. Adv.*, 2021, **7**, eabg1600.
4 S. Liu, G. Chen, P. N. Prasad and M. T. Swihart, *Chem. Mater.*, 2011, **23**, 4098–4101.
5 F. A. A. Nugroho, B. Iandolo, J. B. Wagner and C. Langhammer, *ACS Nano*, 2016, **10**, 2871–2879.
6 R. Strobel and S. E. Pratsinis, *J. Mater. Chem.*, 2007, **17**, 4743–4756.
7 Z. Lin, J. Yue, L. Liang, B. Tang, B. Liu, L. Ren, Y. Li and L. Jiang, *Appl. Surf. Sci.*, 2020, **504**, 144461.
8 *Spark Ablation: Building Blocks for Nanotechnology*, ed. A. Schmidt-Ott, Jenny Stanford Publishing, 2020.
9 S. Schwyn, E. Garwin and A. Schmidt-Ott, *J. Aerosol Sci.*, 1988, **19**, 639–642.
10 A. Kohut, V. Horváth, Z. Pápa, B. Vajda, J. Kopniczky, G. Galbács and Z. Geretovszky, *Nanotechnology*, 2021, **32**, 395501.
11 M. Vazquez-Pufleau, I. Gomez-Palos, L. Arévalo, J. García-Labanda and J. J. Vilatela, *Adv. Powder Technol.*, 2023, **34**, 103955.
12 B. O. Meuller, M. E. Messing, D. L. J. Engberg, A. M. Jansson, L. I. M. Johansson, S. M. Norlén, N. Tureson and K. Deppert, *Aerosol Sci. Technol.*, 2012, **46**, 1256–1270.
13 D. Megyeri, A. Kohut and Z. Geretovszky, *J. Aerosol Sci.*, 2021, **154**, 105758.
14 R. T. Hallberg, L. Ludvigsson, C. Preger, B. O. Meuller, K. A. Dick and M. E. Messing, *Aerosol Sci. Technol.*, 2018, **52**, 347–358.
15 T. V. Pfeiffer, J. Feng and A. Schmidt-Ott, *Adv. Powder Technol.*, 2014, **25**, 56–70.
16 J. Feng, D. Chen, P. V. Pikhitsa, Y. ho Jung, J. Yang and M. Choi, *Matter*, 2020, **3**, 1646–1663.
17 M. Snellman, N. Eom, M. Ek, M. E. Messing and K. Deppert, *Nanoscale Adv.*, 2021, **3**, 3041–3052.
18 S. M. Franzén, L. Jönsson, P. Ternero, M. Kåredal, A. C. Eriksson, S. Blomberg, J. M. Hübner and M. E. Messing, *Nanoscale Adv.*, 2023, **5**, 6069–6077.
19 V. Olszok, P. Rembe, T. Grieb, E. J. Wijeyeratnam, A. Rosenauer and A. P. Weber, *Nanoscale Adv.*, 2024, **6**, 3895–3903.
20 A. Kohut, L. P. Villy, A. Kéri, Á. Bélteki, D. Megyeri, B. Hopp, G. Galbács and Z. Geretovszky, *Sci. Rep.*, 2021, **11**, 5117.
21 L. P. Villy, A. Kohut, A. Kéri, Á. Bélteki, G. Radnóczi, Z. Fogarassy, G. Z. Radnóczi, G. Galbács and Z. Geretovszky, *Sci. Rep.*, 2022, **12**, 1–9.
22 N. S. Tabrizi, Q. Xu, N. M. Van Der Pers, U. Lafont and A. Schmidt-Ott, *J. Nanopart. Res.*, 2009, **11**, 1209–1218.
23 N. S. Tabrizi, Q. Xu, N. M. Van Der Pers and A. Schmidt-Ott, *J. Nanopart. Res.*, 2010, **12**, 247–259.
24 J. Feng, R. Geutjens, N. V. Thang, J. Li, X. Guo, A. Kéri, S. Basak, G. Galbács, G. Biskos, H. Nirschl, H. W. Zandbergen, E. Brück and A. Schmidt-Ott, *ACS Appl. Mater. Interfaces*, 2018, **10**, 6073–6078.
25 J. Feng, N. Ramlawi, G. Biskos and A. Schmidt-Ott, *Aerosol Sci. Technol.*, 2018, **52**, 505–514.
26 P. Ternero, M. Sedrpooshan, D. Wahlqvist, B. O. Meuller, M. Ek, J. M. Hübner, R. Westerström and M. E. Messing, *J. Aerosol Sci.*, 2023, **170**, 106146.
27 L. Jönsson, M. Snellman, A. C. Eriksson, M. Kåredal, R. Wallenberg, S. Blomberg, A. Kohut, L. Hartman and M. E. Messing, *J. Aerosol Sci.*, 2024, **177**, 106333.
28 D. O. de Zárate, C. García-Meca, E. Pinilla-Cienfuegos, J. A. Ayúcar, A. Griol, L. Bellières, E. Hontañón, F. E. Kruis and J. Martí, *Nanomaterials*, 2020, **10**, 466.
29 A. Kohut, L. P. Villy, G. Kohut, G. Galbács and Z. Geretovszky, *Appl. Spectrosc.*, 2023, **77**, 1401–1410.
30 D. B. Williams and C. B. Carter, *Transmission Electron Microscopy: A Textbook for Materials Science*, 2009, pp. 1–760.
31 A. Kohut, G. Galbács, Z. Márton and Z. Geretovszky, *Plasma Sources Sci. Technol.*, 2017, **26**, 045001.
32 A. Kohut, L. Ludvigsson, B. O. Meuller, K. Deppert, M. E. Messing, G. Galbács and Zs. Geretovszky, *Nanotechnology*, 2017, **28**, 475603.
33 C. M. Cundall and J. D. Craggs, *Spectrochim. Acta*, 1955, **7**, 149–164.
34 J. M. Palomares, A. Kohut, G. Galbács, R. Engeln and Z. Geretovszky, *J. Appl. Phys.*, 2015, **118**, 233305.